ORIGINAL ARTICLE

Dual-targeting prodrug nanotheranostics for NIR-II fluorescence imaging-guided photo-immunotherapy of glioblastoma

Fenglin Li[a,†], Yi Lai[b,†], Jiayi Ye[b,†], Madiha Saeed[b], Yijing Dang[a], Zhifeng Zou[a], Fangmin Chen[b], Wen Zhang[a], Zhiai Xu[a,*]

[a]School of Chemistry and Molecular Engineering, East China Normal University, Shanghai 200241, China
[b]State Key Laboratory of Drug Research & Center of Pharmaceutics, Shanghai Institute of Materia Medica, Chinese Academy of Sciences, Shanghai 201203, China

Abstract Glioblastoma (GBM) therapy is severely impaired by the blood−brain barrier (BBB) and invasive tumor growth in the central nervous system. To improve GBM therapy, we herein presented a dual-targeting nanotheranostic for second near-infrared (NIR-II) fluorescence imaging-guided photo-immunotherapy. Firstly, a NIR-II fluorophore MRP bearing donor-acceptor-donor (D-A-D) backbone was synthesized. Then, the prodrug nanotheranostics were prepared by self-assembling MRP with a pro-drug of JQ1 (JPC) and T7 ligand-modified PEG$_{5k}$-DSPE. T7 can cross the BBB for tumor-targeted delivery of JPC and MRP. JQ1 could be restored from JPC at the tumor site for suppressing interferon gamma-inducible programmed death ligand 1 expression in the tumor cells. MRP could generate NIR-II fluorescence to navigate 808 nm laser, induce a photothermal effect to trigger *in-situ* antigen release at the tumor site, and ultimately elicit antitumor immunogenicity. Photo-immunotherapy with JPC and MRP dual-loaded nanoparticles remarkably inhibited GBM tumor growth *in vivo*. The dual-targeting nanotheranostic might represent a novel nanoplatform for precise photo-immunotherapy of GBM.

---

*Corresponding author. Tel./fax: +86 21 54340053.

E-mail address: zaxu@chem.ecnu.edu.cn (Zhiai Xu).

[†]These authors made equal contributions to this work.

1. Introduction

Glioblastoma (GBM) is one of the most aggressive intracranial tumors with high lethality rate[1,2]. Nowadays, surgical resection assisted with radiotherapy or chemotherapy is the standard of care for GBM therapy[3]. However, complete resection of the tiny tumors is challenged by high infiltration and invasiveness of GBM, which accounts for post-operative tumor recurrence[4]. Furthermore, therapeutic delivery to the GBM is restricted by the blood−brain barrier (BBB), which severely impairs GBM therapy[5,6].

In past years, immunotherapy has been extensively exploited for cancer management by eliciting robust and systemic antitumor immune responses[7−11]. Immune checkpoint blockade (ICB) therapy with monoclonal antibody-based immune checkpoint inhibitors efficiently restores the antitumor−immunity cycle *via* reactivating the cytotoxic T lymphocytes (CTLs)[12−18]. However, current ICB therapy suffers from inadequate immunogenicity and acquired immune resistance in GBM. Furthermore, the GBM tumor displays an immunosuppressive tumor microenvironment (ITM) and inadequate intracranial infiltration of T lymphocytes[19,20]. It remains a priority to develop novel therapeutic approaches for synergistically inducing antitumor immunogenicity and normalizing the ITM[21].

Phototherapy, in particular, photothermal therapy (PTT) has been demonstrated to ablate the tumor cells by inducing hyperthermia effect[22−24]. For instance, inorganic nanomaterials or organic molecules with photo-absorbance in the near-infrared (NIR) window have been investigated for PTT *in vitro* and *in vivo*[25−29]. Apart from photothermal ablation of the tumor cells, PTT has recently been demonstrated to elicit antitumor immunity by releasing antigen at the tumor site and recruiting the tumor-infiltrating CTLs[30]. However, PTT of the GBM is challenged by tumor-targeted delivery of the photoabsorbent due to the presence of the BBB. For efficient drug delivery to the GBM tumor, ligand-modified nanomaterials have been developed to traverse the BBB[31−36]. For instance, a T7 peptide (His-Ala-Ile-Tyr-Pro-Arg-His) was demonstrated to enhance BBB penetration of the nanoparticles by recognizing the over-expressed transferrin (Tf) receptors on the brain capillary endothelial cells (BCECs)[37]. T7 ligand is reported to target Tf receptors on the surface of GBM cells[38−40] and, therefore, applied for targeted drug delivery to the GBM tumor. Furthermore, interferon-gamma (IFN-γ) secreted from the tumor-infiltrating CTLs can upregulate PD-L1 in the tumor cells *via* the Janus kinase/signal transducer and activator of transcription (JAK-STAT) pathway, which induces adaptive immunity tolerance of tumor cells[41,42]. In previous studies, we have demonstrated that a potent bromodomain-containing protein 4 (BRD4) inhibitor JQ1 can suppress IFN-γ-inducible PD-L1 expression in the tumor cells[14,15]. However, tumor-specific delivery of JQ1 and BRD4 inhibition remains a prerequisite since BRD4 also serves as a functional protein in the normal tissues.

To this end, we herein proposed a novel nanotheranostic for a second near infrared (NIR-II) fluorescence imaging-guided combinational photo-immunotherapy of GBM. A NIR-II fluorescent probe namely MRP and a reduction-activatable prodrug of JQ1 (namely JPC) were firstly synthesized. MRP, JPC, and T7-modified phospholipid PEG$_{5k}$-DSPE (T7-PEG$_{5k}$-DSPE) were subsequently self-assembled *via* hydrophobic interaction to form a micellar nanoparticle (termed as TNP@JQ1/MRP) (Fig. 1). The resultant TNP@JQ1/MRP nanoparticles can actively be accumulated at the GBM tumor *via* a dual-targeting effect of the T7 peptide. Under the guidance of MRP-performed NIR-II fluorescence imaging, 808 nm laser irradiation can induce a hyperthermia effect to elicit an antitumor immune response and recruit tumor-infiltrating cytotoxic T lymphocytes. Meanwhile, the hyperthermia effect can trigger JQ1 release inside the tumor cells to circumvent IFN-γ-inducible immune evasion. Therefore, the JPC-loaded TNP@JQ1/MRP prodrug nanoparticles cumulatively regressed the GBM tumor by increasing antitumor immunogenicity and overcoming the acquired immune resistance. NIR-II nanotheranostic-based photo-immunotherapy exhibited several advantages over conventional PTT agents. First, T7 ligand-modified prodrug nanoparticles can cross BBB and precisely target the GBM cells for tumor-specific drug delivery. Second, MRP-loaded nanotheranostics can perform NIR-II fluorescence imaging-guided thermal ablation in GBM cells and precise photo-immunotherapy. Furthermore, the prodrug nanoparticles integrating glutathione (GSH)-activatable JPC prodrug and a phase-change material (PCM) can restore and release JQ1 at the tumor site in a hyperthermia tunable manner. JQ1 is able to suppress IFN-γ- inducible PD-L1 expression in the tumor mass by targeting the epigenetic protein BRD4.

2. Materials and methods

2.1. Synthesis of NIR-II fluorophore MRP and JQ1 prodrug JPC

MRP and JPC were synthesized according to the procedures described in the Supporting Information.

2.2. GSH-mediated reduction of JPC

To verify the GSH-mediated disulfide reduction reaction of JPC, JPC (1.0 mg/mL) was incubated with GSH (5.0 mmol/L) in water for 1 h. Then the mixture was monitored by using high-performance liquid chromatography (HPLC) with water/acetonitrile (*v/v*, 95/5) as mobile phase. JQ1-SH was confirmed using electrospray ionization mass spectrometry (ESI-MS) measurement.

2.3. Preparation of the prodrug nanoparticle

To prepare the dual-targeting prodrug nanoparticles, T7-PEG$_{5K}$-DSPE, lecithin and JPC were dissolved in 4% aqueous solution of ethanol at an optimized weight ratio of 1:1.5:1.5 and incubated at 50 °C for 10 min. Subsequently, methanol solution of LA and SA (*w/w*, 4:1) as the PCM with a low melting point at 39 °C and DMF solution of MRP were added under stirring to form the micellar nanoparticles. The nanoparticle suspension was dialyzed against deionized water, and passed through a membrane filter (0.22 μm) to obtain TNP@JQ1/MRP nanoparticles. T7-free NP@JQ1/MRP nanoparticles were prepared as control.

2.4. Physicochemical characterization of the prodrug nanoparticle

Dynamic light scattering (DLS, Nano-Sizer, Malvern, England) and transmission electron microscopy (TEM, Talos L120C, USA) were employed to determine hydrodynamic diameter and morphology of the TNP@JQ1/MRP and NP@JQ1/MRP nanoparticles, respectively. The stability of the nanoparticles was tested in 10% fetal bovine serum (FBS) solution by DLS. The
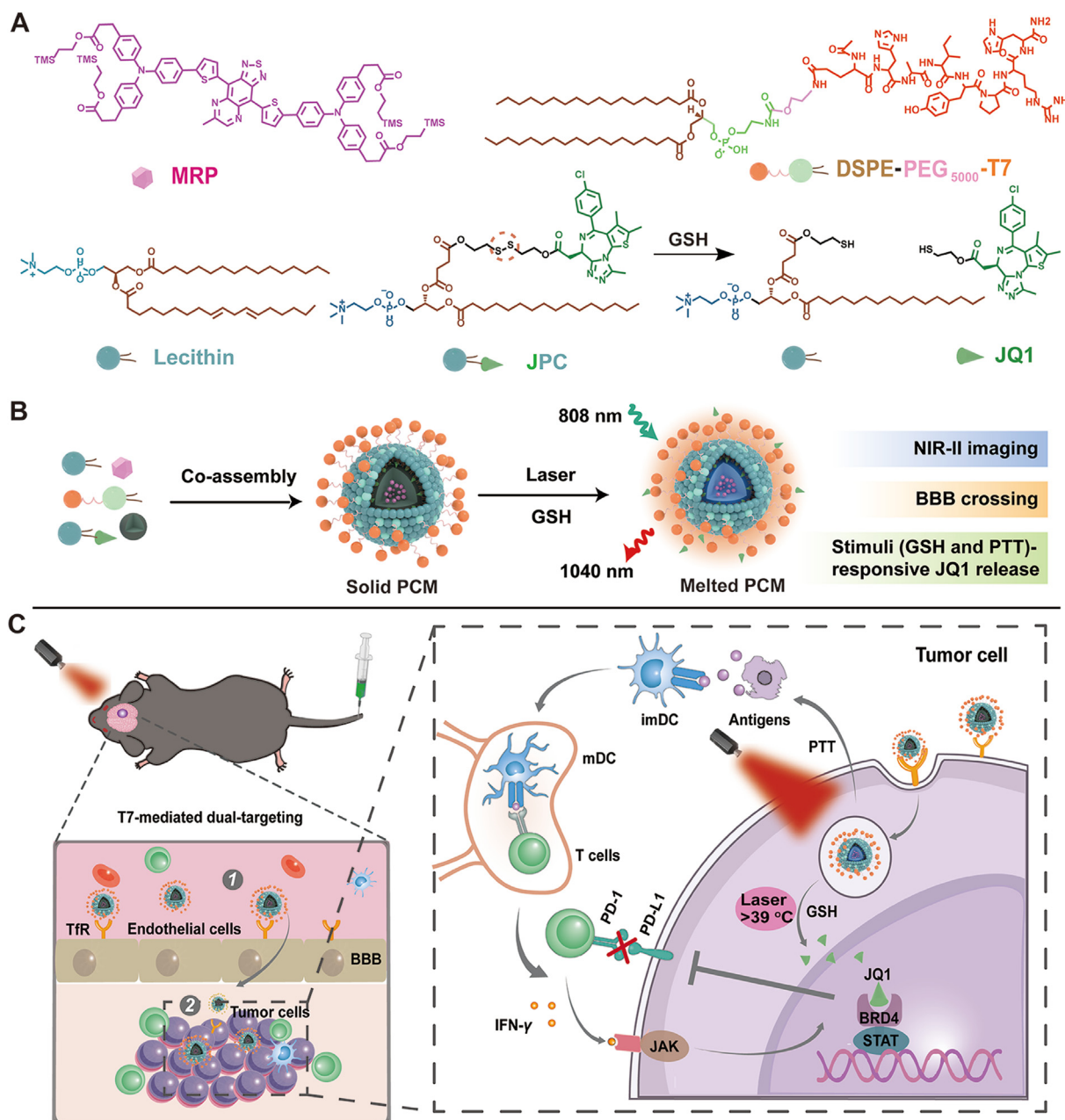
Figure 1 Schematic illustration of prodrug-based nanotheranostics for precise photo-immunotherapy of GBM. (A) Chemical structure of MRP, prodrug JPC, lecithin, and T7-PEG$_{5k}$-DSPE. (B) Self-assembly of the prodrug nanotheranostic. (C) Schematic demonstration of the prodrug-based nanotheranostic approach for photo-immunotherapy. Firstly, the prodrug nanotheranostic traversed BBB and precisely accumulated at the GBM area by Tf receptor-mediated endocytosis and exocytosis. Upon NIR-II fluorescence imaging navigation, the prodrug nanotheranostic performed excellent photothermal ability under 808 nm laser for inducing photothermal ablation of GBM cells and released tumor-associated antigens for eliciting an antitumor immune response.

absorbance and fluorescence spectra of NP@JQ1/MRP and MRP were recorded by UV–Vis (Cary 60, USA) and fluorescence spectrophotometer (λ_{Ex} = 808 nm, λ_{Em} = 850–1500 nm, FLS 980, Edinburgh Instruments, UK), respectively. The loading efficiency (DL%) and encapsulation efficiency (EE%) of MRP and JPC were calculated by UV–Vis spectrometer and HPLC, respectively. To examine the reduction-sensitive property, prodrug nanoparticles were included with 5.0 mmol/L of GSH and irradiated with 808 nm laser at photodensity of 1.5 W/cm^2. Reduction

of the disulfide bond was monitored by HPLC (elute: water/acetonitrile (v/v, 95/5) at a flow rate of 0.5 mL/min).

2.5.   Photothermal performance of NP@JQ1/MRP

To measure photothermal performance of the NP@JQ1/MRP nanoparticles, aqueous suspensions of NP@JQ1/MRP at pre-determined MRP concentrations (0–65 µmol/L) were treated with 808 nm laser at photodensity of 0.5, 1.0, 1.5 or 2.0 W/cm^2. Laser

irradiation-induced temperature elevation was monitored with an IR camera (AI150-15-M, Shanghai IR Tech Co., Ltd., China).

2.6. Cellular uptake of the dual-targeting TNP@JQ1/DiI nanoparticles

To investigate cellular uptake of prodrug nanoparticles, G422 mouse glioma cells were cultured in 6-well plate and treated with TNP@JQ1/DiI or NP@JQ1/DiI nanoparticles at an identical DiI concentration of 2.0 μmol/L. The intracellular fluorescence signal of DiI was tested by flow cytometry assay (BD FACS Calibur, USA).

To exploit intracellular distribution of TNP@JQ1/DiI nanoparticles, G422 tumor cells were incubated on coverslip in 24-well tissue culture plate. After 24 h, G422 cells were incubated with TNP@JQ1/DiI or NP@JQ1/DiI for 2 h at a DiI concentration of 2.0 μmol/L. The cells were subsequently stained with DAPI, fixed with 4% paraformaldehyde, and examined by confocal laser scanning microscopy (CLSM, Leica TCS-SP8, Germany).

To elucidate active tumor-targeting effect of the T7-modified nanoparticles, G422 tumor cells were pre-treated with free T7, then incubated with the TNP@JQ1/DiI nanoparticles. The cells were examined by flow cytometry and CLSM, respectively. To investigate dual-targeting ability of the nanoparticles, TNP@JQ1/DiI nanoparticles were incubated with 3T3 cells, bEnd.3 cells or G422 cells for 2 h. Intracellular fluorescence intensity was then detected by flow cytometry.

2.7. Cytotoxicity of the TNP@JQ1/MRP nanoparticles

G422 cells were incubated in a 96-well plate. After 24 h, the cells were then incubated with TNP@JQ1/MRP and other nanoparticles of different concentrations for 24 h. Cell vitality was tested using CCK-8 assay.

To investigate phototoxicity of prodrug nanoparticles in vitro, G422 cells were cultured with TNP@JQ1/MRP or NP@JQ1/MRP nanoparticles at MRP concentrations of 20 or 40 μmol/L for 24 h. The cells were then irradiated with 808 nm laser for 5 min. The cell vitality was examined using CCK-8 assay.

2.8. DC maturation in vitro

To investigate photo-immunotherapy induced immune response, bone marrow dendritic cells (BMDCs) were extracted from C57/BL6 mice, and stimulated with interleukin-4 (IL-4, 10.0 ng/mL) and mouse recombinant GM-CSF (20.0 ng/mL) for a week. G422 cells were cultured with the prodrug nanoparticles ($C_{MRP} = 40$ μmol/L). After 12 h, G422 cells were illuminated with 808 nm laser for 5 min at photodensity of 2.0 W/cm^2. The cells were subsequently incubated for additional 4 h. The BMDCs were then incubated with the pre-treated tumor cells for 24 h. DC maturation were examined via flow cytometry assay.

2.9. IFN-γ-inducible PD-L1 expression

G422 cells were seeded in 6-well tissue culture plate and incubated for 24 h. The cells were treated with IFN-γ at different concentrations (0, 10, 50, 100, 200 ng/mL) for 24 h. The cells were then stained with anti-CD274-APC for 30 min and examined by flow cytometry and Western blot (WB) assay. The protein image was taken using the Tanon-5200 imaging system (Tanon, Shanghai, China).

To investigate the effect of JQ1 or TNP@JQ1 on PD-L1 expression, G422 cells were treated with IFN-γ for 24 h at the desired concentration (e.g., 50 ng/mL). G422 cells were then treated with JQ1 or TNP@JQ1 for additional 24 h at an identical JQ1 concentration of 1 μmol/L. The cells were finally stained with anti-CD274-APC for flow cytometry assay and harvested for WB assay.

2.10. Cell lines, animals and tumor model

Murine G422 cells and Luciferase expressing G422 (G422-Luc) tumor cells were obtained from Fudan University (Shanghai, China). Murine fibroblast 3T3 and brain microvascular endothelial bEnd.3 cells were obtained from the cell bank of Chinese Academy of Sciences (Shanghai, China). G422, G422-Luc, 3T3 and bEnd.3 cells were all maintained in 10% (v/v) FBS-containing DMEM cell culture medium at 37 °C under a humidified atmosphere with 5% of CO$_2$ supply.

BALB/c nude mice (female, 4−5 weeks old) and C57/BL6 mice (female, 4−5 weeks old) were obtained from Shanghai Experimental Animal Center (Shanghai, China). Animal experiments were conducted under the guidelines approved by the Institutional Animal Care and Use Committee (IACUC) of Shanghai Institute of Materia Medica (2021-09-YHJ-06), China.

To establish an orthotopic GBM tumor model, G422-Luc cells (1×10^5 cells in 5.0 μL of PBS) were implanted into the brain striatum of BALB/c nude mouse. Tumor growth was monitored via bioluminescence imaging (BLI) in vivo. To establish a subcutaneous GBM tumor model, G422 cells (3×10^6 cells in 100 μL of PBS) were injected into right forelimb of C57/BL6 mice.

2.11. Bioluminescence and fluorescence imaging for orthotopic model in vivo

To exploit biodistribution of the prodrug nanoparticles in vivo, G422-Luc tumor-bearing mice were intravenously (i.v.) injected with TNP@JQ1/DiR and NP@JQ1/DiR nanoparticles at a DiR dose of 0.25 mg/kg. The mice were then pretreated with D-luciferin potassium salt for 10 min and imaged by IVIS Spectrum CT (PerkinElmer, Waltham, USA). Then fluorescence imaging of complete mice in vivo and brain ex vivo was all presented by an IVIS Spectrum CT at different times. After 36 h injection, the brains were harvested and fixed in 4% formalin solution to use.

To investigate tumor accumulation of TNP@JQ1/MRP and NP@JQ1/MRP in vivo, tumor-bearing nude mice were i.v. injected with TNP@JQ1/MRP or NP@JQ1/MRP nanoparticles at an equal MRP dose of 2.5 mg/kg. NIR-II fluorescence imaging of brain was performed in vivo and ex vivo with the MARS imaging system, which was equipped with an InGaAs camera and shadowless illumination with an 808 nm laser, 850 nm long pass filter and 50 ms of exposure time.

2.12. Fluorescence imaging of the subcutaneous glioma tumor in vivo

To investigate tumor-targeted distribution of prodrug nanoparticles in vivo, C57/BL6 mice bearing subcutaneous G422 tumor were i.v. injected with TNP@JQ1/MRP and NP@JQ1/MRP at a MRP dose of 2.5 mg/kg. NIR-II fluorescence images were subsequently performed with the MARS imaging system.

2.13. Photothermal efficacy of the prodrug nanoparticles

To investigate photothermal efficacy of prodrug nanoparticles in vivo, C57/BL6 mice bearing G422 subcutaneous tumor were i.v.

injected with PBS, NP@JQ1/MRP or TNP@JQ1/MRP nanoparticles at an identical MRP dose of 2.5 mg/kg. The mice were then illuminated with 808 nm laser for 6 min (1.0 W/cm^2) at 36 h post-injection. Laser irradiation-induced temperature elevation was monitored with an IR thermal camera.

2.14. Antitumor performance of the TNP@JQ1/MRP nanoparticles

The C57/BL6 mice bearing subcutaneous G422 tumor were randomly separated into five groups ($n = 6$) and i.v. injected with PBS, TNP@JQ1, TNP/MRP, TNP@JQ1/MRP, TNP@JQ1/MRP at a JQ1 dose of 15 mg/kg and MRP dose of 2.5 mg/kg, respectively. The tumors of the TNP/MRP and TNP@JQ1/MRP groups were illuminated with 808 nm laser (1.0 W/cm^2, 10 min) at 36 h post-injection. The treatment was repeated for three times every 3-days and repeated triplicates in total. The tumor volume and body weight were recorded during the antitumor study. The tumor volume was calculated with Eq. (1):

$$V = L \times W \times W/2 \tag{1}$$

where L presents the longest dimension, W presents the shortest dimension).

The mice were determined dead according to the animal ethics when the tumor volume reached 2000 mm^3. The tumors and organs including hearts, livers, lungs, spleens and kidneys were collected at the end of experiment, fixed in 4% formalin solution and exposed to haematoxylin and eosin (H&E) staining.

2.15. DC maturation and intratumoral infiltration of T lymphocytes in vivo

To analyze the mechanism of excellent antitumor effect induced by nanoparticles, mice subcutaneously inoculated with G422 cells were separated to five groups ($n = 3$): (i) PBS; (ii) TNP@JQ1; (iii) TNP/MRP + Laser; (iv) TNP@JQ1/MRP; (v) TNP@JQ1/MRP + Laser. 808 nm laser illumination (1.0 W/cm^2, 10 min) at the tumor site was carried out at 36 h post-injection. The frequency of administration was once every 3 days and treatment 3 times in total. After treatment 3 times, all the tumor and lymph nodes (LNs) were obtained for subsequent measurements of immune cells infiltrating.

2.16. PD-L1 expression in subcutaneous G422 model

To explore PD-L1 expression in the tumor tissues, C57/BL6 mice bearing G422 subcutaneous tumor were i.v. injected with PBS, TNP@JQ1, TNP/MRP + Laser, TNP@JQ1/MRP or TNP@JQ1/MRP + Laser at a JQ1 dose of 15 mg/kg and MRP dose of 2.5 mg/kg, respectively. The tumors were then illuminated under 808 nm laser (1.0 W/cm^2) at 36 h post-injection. The tumors were harvested post treatment, fixed with 4% formalin and examined by immunofluorescence staining *ex vivo*.

3. Results and discussion

3.1. Preparation and characterization of TNP@JQ1/MRP

NIR-II fluorescence imaging shows deep tissue penetration and improves signal-to-background contrast, which is desirable for fluorescence imaging of the brain *in vivo*[43]. Compared to nanomaterial-based NIR-II fluorescent probes (*e.g.*, carbon nanotubes and quantum dots), small molecular fluorophores bearing donor-acceptor-donor (D-A-D) scaffold display large stokes shift, high photostability, and good biosafety, which are more favorable for biomedical applications[44]. In this study, the D-A-D type fluorophore MRP was synthesized by a Maillard-like reaction between methylglyoxyl and thiadiazole-fused *o*-phenylenediamine (Supporting Information Scheme S1). The thiadiazole-fused quinoxaline was employed as an electron-deficient block. The successful synthesis of MRP was validated by a hydrogen nuclear magnetic resonance (^{1}H-NMR) spectrometer (Supporting Information Figs. S1–S3). MRP displayed maximum absorption at 730 nm and maximum fluorescence emission at ∼1060 nm (Fig. 2A and B), verifying its potential for NIR-II fluorescence imaging *in vivo*.

JQ1 is a potent BRD4 inhibitor, which can abolish IFN-γ-inducible PD-L1 upregulation in the tumor cells to prevent adaptive immunity evasion[45]. To achieve intratumor-specific delivery of JQ1, the reduction-sensitive JPC prodrug was synthesized by grafting JQ1 onto the hydroxyl group of 1-palmitoyl-2-hydroxy-*sn*-glycero-3-phosphocholine (P-lysoPC) with a disulfide spacer. The chemical structure of JPC was confirmed by ^{1}H-NMR and ESI-MS characterization (Supporting Information Figs. S4–S7). JQ1-SH was released from JPC in 60 min when incubated with GSH as determined by HPLC and ESI-MS measurements (Supporting Information Fig. S8), validating the superior reduction sensitivity of JPC.

It was reported that LA and SA formed PCM at a mass ratio of 4:1 for hyperthermia-triggered drug release[46,47]. In this study, MRP, and JPC dual-loaded prodrug nanoparticles were prepared by self-assembly of MRP, JPC, LA, SA, T7-PEG$_{5k}$-DSPE and lecithin *via* hydrophobic interaction. The composition of the nanoparticles was optimized by screening JPC and MRP feeding ratio (Supporting Information Tables S1 and S2). Successful loading of JPC and MRP inside the hydrophobic core of the nanoparticles was verified by UV–Vis spectra and HPLC measurement. The EE% of JPC and MRP was determined to be $86.2 \pm 2.1\%$ and $75.2 \pm 1.6\%$, respectively. The JPC and MRP loading capacity was $10.7 \pm 0.2\%$ and $2.5 \pm 0.2\%$ (Supporting Information Figs. S9 and S10). The JPC and MRP co-loaded prodrug nanoparticles were named as NP@JQ1/MRP. T7-modified nanoparticles (namely TNP@JPC/MRP) were prepared by replacing PEG$_{5k}$-DSPE with T7-PEG$_{5k}$-DSPE. DLS and TEM characterizations showed that NP@JQ1/MRP and TNP@JQ1/MRP had a hydrodynamic diameter of 110–140 nm and narrow particle size polydispersity index (PDI <0.2, Fig. 2C–E and Supporting Information Fig. S11). MRP encapsulating nanoparticles displayed strong absorbance and slight blue-shift of fluorescence emission ($E_{max} = 975$ nm, Fig. 2A and B). Notably, both NP@JQ1/MRP and TNP@JQ1/MRP nanoparticles showed good colloidal stability in a 10% FBS-containing cell culture medium (Supporting Information Fig. S11 and Fig. 2F).

The photothermal effect of the MRP-loaded nanoparticles was next assessed under 808 nm laser irradiation, in which aqueous dispersions of nanoparticles showed remarkable temperature elevation in a MRP concentration- and photodensity-dependent manner (Fig. 2G and H, Supporting Information Fig. S12). For example, upon 808 nm laser irradiation for 9 min, the temperature of MRP-loaded nanoparticle suspension increased from 20 to 58 °C at 65 μmol/L of MRP and 1.5 W/cm^2, suggesting the promising potential of the TNP@JQ1/MRP nanoparticles for photothermal ablation of the tumor cells.
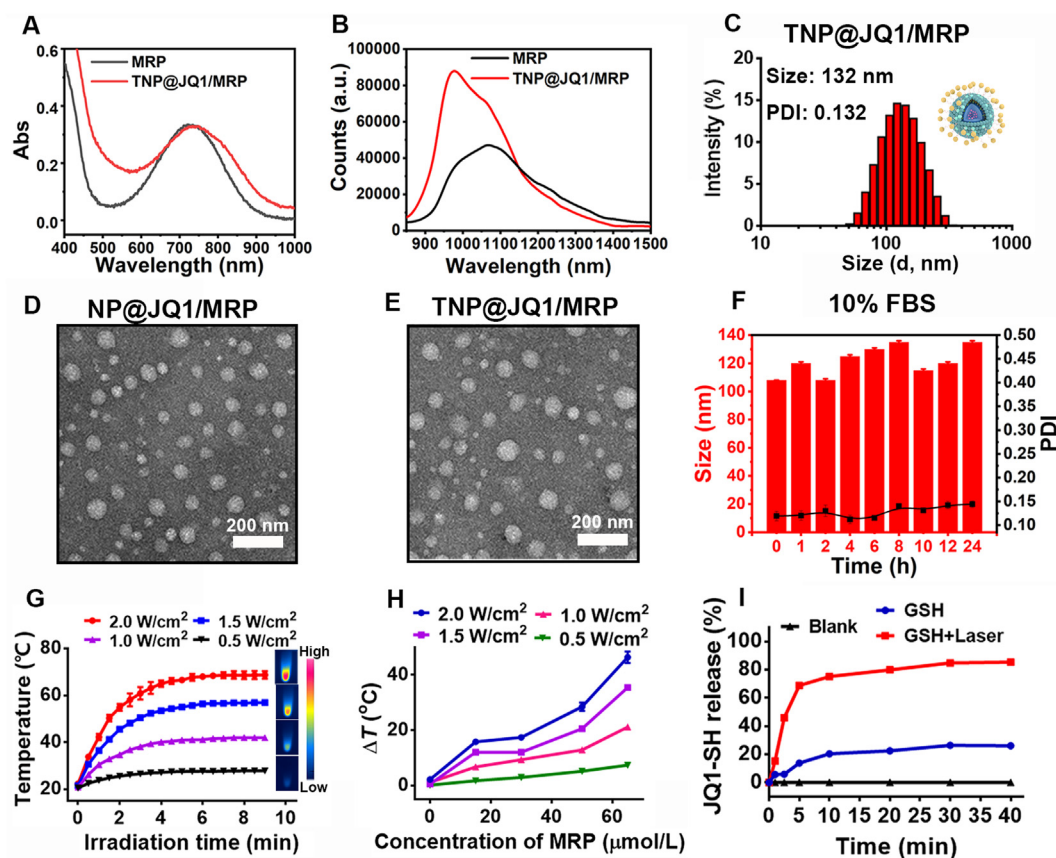
Figure 2 Physicochemical characterization of prodrug nanoparticles. (A) Absorbance and (B) fluorescence spectra of MRP in DMF and MRP-loaded nanoparticles in water. (C) DLS-determined hydrodynamic diameter of the TNP@JQ1/MRP nanoparticles. (D) and (E) TEM images of NP@JQ1/MRP and TNP@JQ1/MRP nanoparticles. (F) Serum stability of TNP@JQ1/MRP nanoparticles in 10% of FBS. (G) and (H) Photo-thermal effect of the NP@JQ1/MRP nanoparticles as a function of (G) photodensity (MRP concentration at 65 μmol/L), and (H) photodensity and MRP concentration. (I) JQ1 release from NP@JQ1/MRP (65 μmol/L of MRP) nanoparticle induced by GSH (5.0 mmol/L) and laser irradiation (photodensity of 1.5 W/cm^2).

To quantify the JQ1 release profile *in vitro*, the NP@JQ1/MRP nanoparticles were incubated with 5.0 mmol/L GSH and illuminated with 808 nm NIR laser. The result displayed that leakage of JQ1 from nanoparticles was 24.0 ± 0.3% after 40 min, verifying the reduction-elicited JQ1 leakage property of nanoparticles. In contrast, 85.2 ± 0.3% of JQ1 was released from the nanoparticles under laser irradiation at 1.5 W/cm^2 after 40 min incubation with 5.0 mmol/L GSH (Fig. 2I). This could be attributed to GSH-inducible dissociation of disulfide bond as well as photo hyperthermia-induced phase transition of the PCM.

3.2. Tumor targeting, cytotoxicity, and DC maturation assay

To evaluate the active tumor-targeting profile of the prodrug nanoparticles, G422 cells were firstly incubated with TNP@JQ1/DiI nanoparticles for 2 h. CLSM examination displayed significantly higher intracellular DiI fluorescence in the TNP@JQ1/DiI group compared to that of the NP@JQ1/DiI control group (Fig. 3A). The intracellular fluorescence signal dramatically declined when the cells were pre-treated with free T7 peptide to block the Tf receptor. Quantitative assay by flow cytometry further validated 3.0-fold stronger intracellular uptake of TNP@JQ1/DiI than NP@JQ1/DiI (Fig. 3B). Remarkably, intracellular uptake of the TNP@JQ1/DiI nanoparticles was suppressed by pre-treating

the tumor cells with T7 ligand, validating T7-mediated tumor targeting of the TNP@JQ1/DiI nanoparticles.

Next, we investigated the dual-targeting ability of the TNP@JQ1/MRP in three cell lines, including G422, mouse fibroblast cell (3T3), and murine brain microvascular endothelial cell (bEnd.3), respectively. Flow cytometry assays showed 2.3- and 2.6-fold higher intracellular DiI fluorescence intensity in G422 cells and bEnd.3 cells than that of the 3T3 cells, suggesting the potential of the T7-modified nanoparticles in targeting the bEnd.3 *via* crossing the BBB (Fig. 3C).

Given the endothelia and G422 cells' dual-targeting profile of the prodrug nanoparticles, we next evaluated their cytotoxicity and photo-cytotoxicity in the G422 cells *in vitro*. CCK-8 assay revealed negligible cytotoxicity of the JQ1 prodrug and MRP dual-loaded prodrug nanoparticles (Supporting Information Fig. S13). In contrast, upon 808 nm laser irradiation, the TNP@JQ1/MRP nanoparticles induced much higher photo-cytotoxicity than the NP@JQ1/MRP nanoparticles (Fig. 3D and E). The increased photo-cytotoxicity of the prodrug nanoparticles could be attributed to T7 ligand-promoted intracellular uptake of the TNP@JQ1/MRP nanoparticles.

Dendritic cells (DCs) are critical antigen presentation cells for antigen uptake and presentation to the T lymphocytes. We thus investigated whether the TNP@JQ1/MRP nanoparticles elicit an
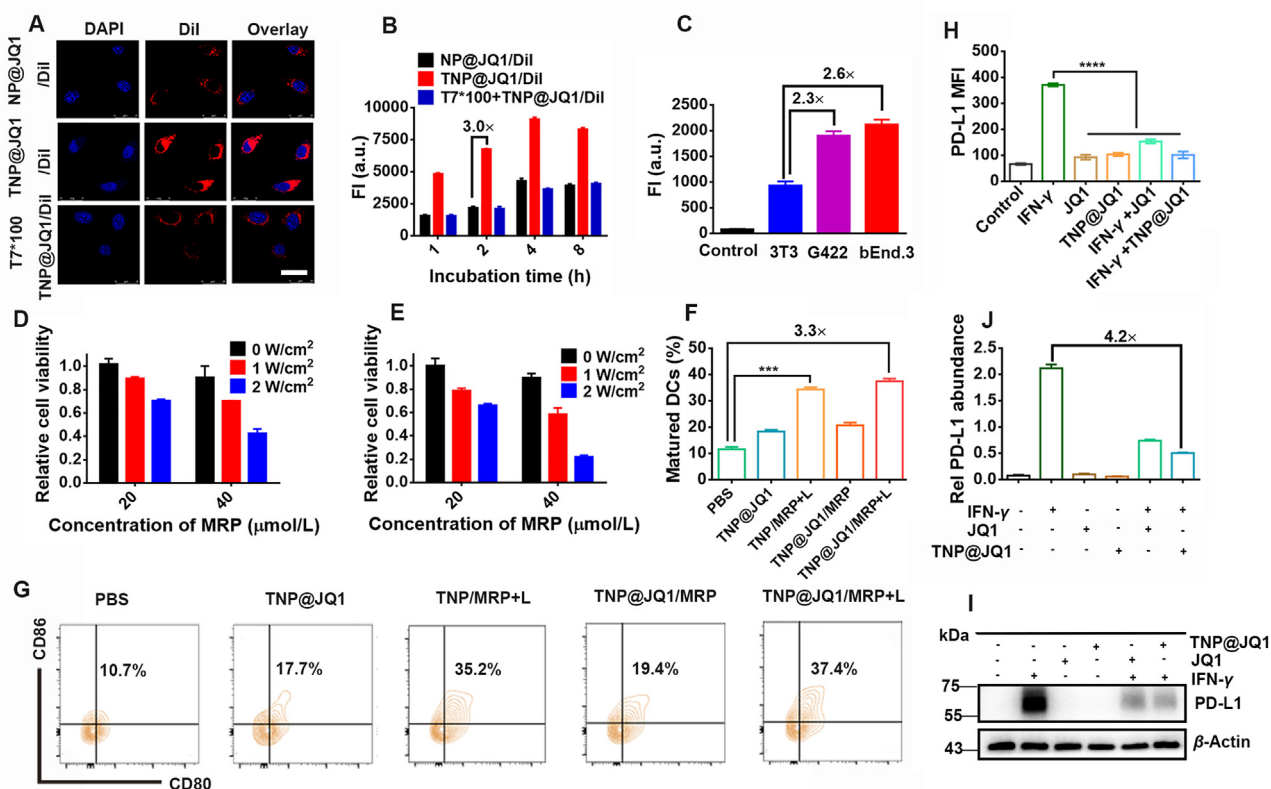
Figure 3 Cellular uptake and cytotoxicity of TNP@JQ1/MRP nanoparticles. (A) CLSM examination of different nanoparticles in G422 cells (scale bar = 25 μm). (B) Flow cytometry assay of prodrug nanoparticles uptake in G422 cells *in vitro*. (C) Flow cytometric analysis of TNP@JQ1/MRP nanoparticles uptake in 3T3, bEnd.3, and G422 cells. (D) and (E) Phototoxicity of (D) NP@JQ1/MRP, and (E) TNP@JQ1/MRP nanoparticles in G422 cells. (F) G422 cells-induced maturated DCs proportion (gated on CD11c$^+$CD80$^+$CD86$^+$) (*n* = 3), and (G) representative flow cytometric plots. (H) Flow cytometry assay, and (I) WB assay of PD-L1 expression in G422 cells. (J) Semi-quantitation of WB results in (I) by Image J analysis (*n* = 3). Statistical significance: *n* = 3, *$P < 0.05$, **$P < 0.01$, ***$P < 0.001$.

antitumor immune response by examining DC maturation. G422 cells were pre-incubated with the TNP@JQ1/MRP nanoparticles, irradiated with 808 nm laser, and then incubated with DCs for 24 h. Flow cytometry assay displayed that G422 cells pretreated with TNP/MRP + Laser and TNP@JQ1/MRP + Laser significantly promoted DC maturation, which could be attributed to PTT-mediated tumor cell ablation and antigen release. Remarkably, the DCs maturation ratio of TNP@JQ1/MRP + Laser group was 3.3-fold higher than that of PBS group (Fig. 3F and G) due to the increased photothermal effect of the dual-targeting TNP@JQ1/MRP nanoparticles.

IFN-γ-induced upregulation of PD-L1 in the tumor cells can be reverted using JQ1[15]. To investigate whether the prodrug nanoparticles could suppress PD-L1 expression in GBM tumors, G422 cells were pre-cultured with IFN-γ for 24 h. Flow cytometric measurements revealed that IFN-γ elicited PD-L1 expression as a function of concentration, which was further validated by WB assay (Supporting Information Fig. S14).

It was reported that JQ1 inhibits PD-L1 expression *via* blocking BRD4-mediated PD-L1 transcription[45]. We next investigated whether TNP@JQ1 suppressed IFN-γ-induced PD-L1 upregulation in G422 cells. Flow cytometric measurement confirmed that JQ1 and TNP@JQ1 nanoparticles effectively inhibited IFN-γ-induced PD-L1 expression on the surface of G422 cells *in vitro* (Fig. 3H), as further verified by WB assay (Fig. 3I and J).

3.3. NIR-II fluorescence imaging of the orthotopic GBM tumor in vivo

With the dual-targeting TNP@JQ1/MRP prodrug nanoparticles in hand, we next evaluated their ability to perform fluorescence imaging in the NIR-II region. BALB/c nude mice bearing orthotropic G422 tumor were separated into two groups and i. v. injected with NP@JQ1/MRP or TNP@JQ1/MRP nanoparticles. Fluorescence imaging was then performed at pre-determined time points. Fig. 4A and B displayed that the intratumoral fluorescence signal increased over time, peaked at 24 h post-injection and declined thereafter. The fluorescence imaging data indicated that NP@JQ1/MRP and TNP@JQ1/MRP successfully crossed the BBB and accumulated at the tumor site. It was worth noting that the fluorescence intensity in the TNP@JQ1/MRP group was much higher than that of the NP@JQ1/MRP group at all the time points. For example, the TNP@JQ1/MRP group showed a 1.8-fold stronger NIR-II fluorescence signal over the NP@JQ1/MRP group at 24 h and significantly accumulated in the brain (Fig. 4C). This phenomenon validated that the T7 ligand-modification enhanced the BBB penetration and tumor-targeting properties of the TNP@JQ1/MRP nanoparticles.

To investigate whether T7-modified prodrug nanoparticles specifically distributed in the GBM tumor *in vivo*, we used G422-Luc glioma cells to visualize the orthotopic tumor by BLI *in vivo* and *ex-vivo*. By comparison, nanoparticles distribution in the tumor were examined by NIR-I fluorescence imaging with DiR-
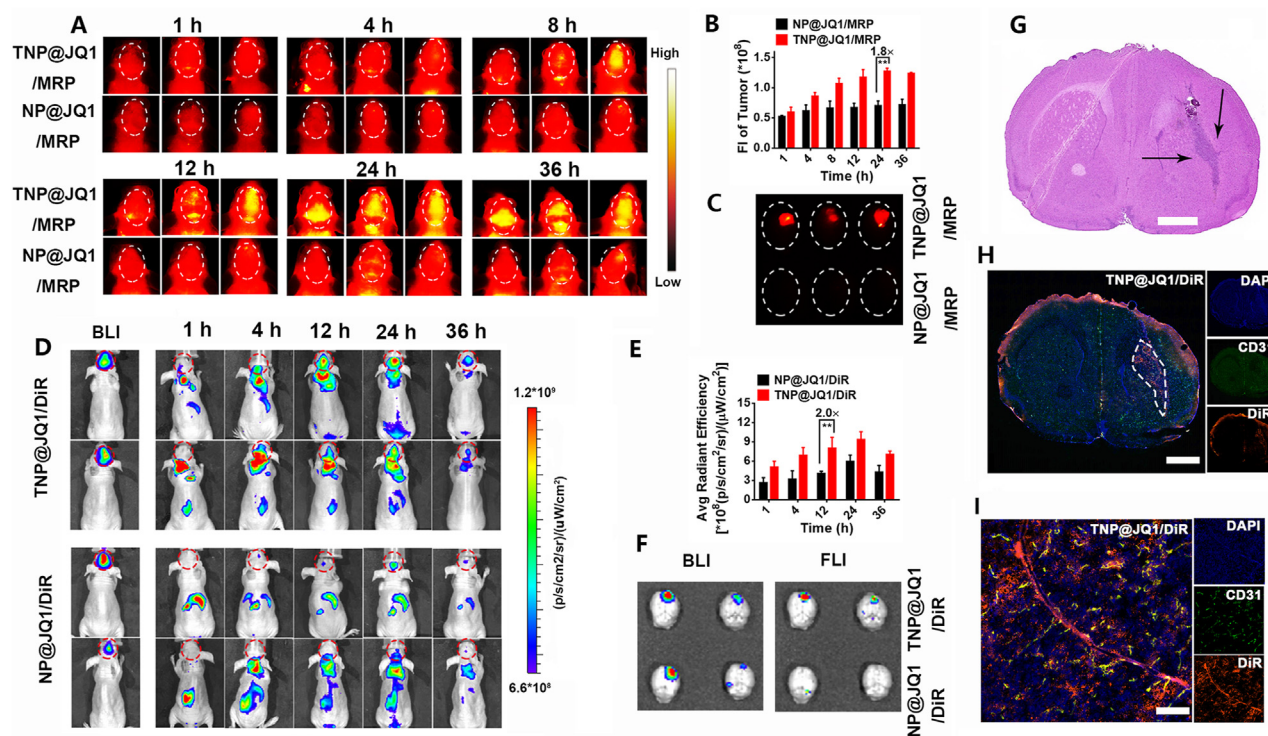
Figure 4 Fluorescence imaging of the nanoparticle distribution *in vivo* and *ex-vivo*. (A) NIR-II fluorescence imaging of TNP@JQ1/MRP nanoparticle distribution *in vivo*. (B) Semi-quantitation of NIR-II fluorescence intensity in the tumor. (C) NIR-II fluorescence imaging of the brain at 36 h post injection *ex-vivo*. (D) NIR-I fluorescence imaging of NP@JQ1/DiR and TNP@JQ1/DiR nanoparticles distribution *in vivo*. (E) Semi-quantification of NIR-I fluorescent intensity in brain. (F) Bioluminescence and NIR-I fluorescent imaging of the brain at 36 h post-injection. (G) H&E staining of the brain section at 36 h post-injection (the dark part indicated the GBM tumor) (scale bar = 1 mm). (H) CLSM examination of TNP@JQ1/DiR distribution in the brain section (scale bar = 1 mm). (I) Enlarged view of the glioma section *ex-vivo* (scale bar = 100 μm). Statistical significance: $n = 3$, *$P < 0.05$, **$P < 0.01$, ***$P < 0.001$.

loaded nanoparticles. Fig. 4D showed that the G422 tumor co-localized well with the fluorescence signal *in vivo*. The TNP@JQ1/DiR nanoparticles attained 2.0-fold stronger orthotopic tumor fluorescence intensity than their NP@JQ1/DiR counterpart at 12 h post-injection (Fig. 4E). Tumor-specific distribution of the TNP@JQ1/DiR nanoparticles was further validated by BLI and fluorescence imaging of the brain tissue *ex-vivo* (Fig. 4F), suggesting a crucial role of T7 peptide for BBB crossing and tumor-targeted drug delivery *in vivo*.

To further demonstrate the dual-targeting effect of the prodrug nanoparticles, the brain tissue was harvested at 36 h post nanoparticle injection and stained with H&E. TNP@JQ1/DiR nanoparticles dominantly distributed in the glioma tumor (the part outlined by white dotted line), verifying satisfying BBB permeability of the T7-modified nanoparticles, which subsequently diffused throughout the tumor tissue (Fig. 4G−I). Collectively, the BLI and fluorescence imaging data consistently verified the active tumor targeting profile of the T7-modified prodrug nanoparticles *in vivo*.

3.4. Antitumor efficacy of the TNP@JQ1/MRP nanoparticles in vivo

Inspired by the dual-targeting and NIR-II fluorescence emission profile of the TNP@JQ1/MRP nanoparticles, we next evaluated the antitumor performance using the subcutaneous G422 tumor model. Fluorescence imaging illustrated the improved targeting ability of the TNP@JQ1/MRP nanoparticles over the T7-free NP@JQ1/MRP control (Fig. 5A). The semi-quantitative assay

revealed that the TNP@JQ1/MRP group displayed 1.7-fold higher intratumoral fluorescence intensity than the NP@JQ1/MRP group at 24 h post-injection (Fig. 5B).

Subsequently, *in vivo* photothermal effect of MRP-loaded prodrug nanoparticles was assessed. The G422 tumor-bearing mice were i.v. injected with PBS, NP@JQ1/MRP, and TNP@JQ1/MRP nanoparticles and irradiated under an 808 nm laser after 36 h. The tumor temperature of NP@JQ1/MRP-injected mice increased by ∼15 °C upon 6 min laser irradiation. In contrast, the TNP@JQ1/MRP group displayed much higher temperature elevation up to 50 °C due to increased intratumoral accumulation of the dual-targeting nanoparticles (Fig. 5C). The remarkable hyperthermia effect of the TNP@JQ1/MRP nanoparticles suggested their potential for PTT of the GBM tumor.

To evaluate the antitumor efficacy of the prodrug nanoparticles, mice inoculated with G422 cells were arbitrarily separated into five groups. The mice were injected with PBS, TNP@JQ1, TNP/MRP or TNP@JQ1/MRP nanoparticles by tail vein every three days for three times (Fig. 5D). After 36 h, the mice of the TNP/MRP and TNP@JQ1/MRP groups were treated under 808 nm laser irradiation (1.0 W/cm²) at 36 h post-injection. TNP@JQ1 and TNP@JQ1/MRP slightly delayed the growth of G422 tumors, and TNP/MRP + Laser showed a moderate antitumor effect (Fig. 5E−G). In contrast, TNP@JQ1/MRP + Laser almost eliminated the G422 tumor and markedly extended the survival of the tumor-bearing mice, indicating remarkably improved antitumor performance of TNP@JQ1/MRP-mediated photo-immunotherapy (Fig. 5G and H).
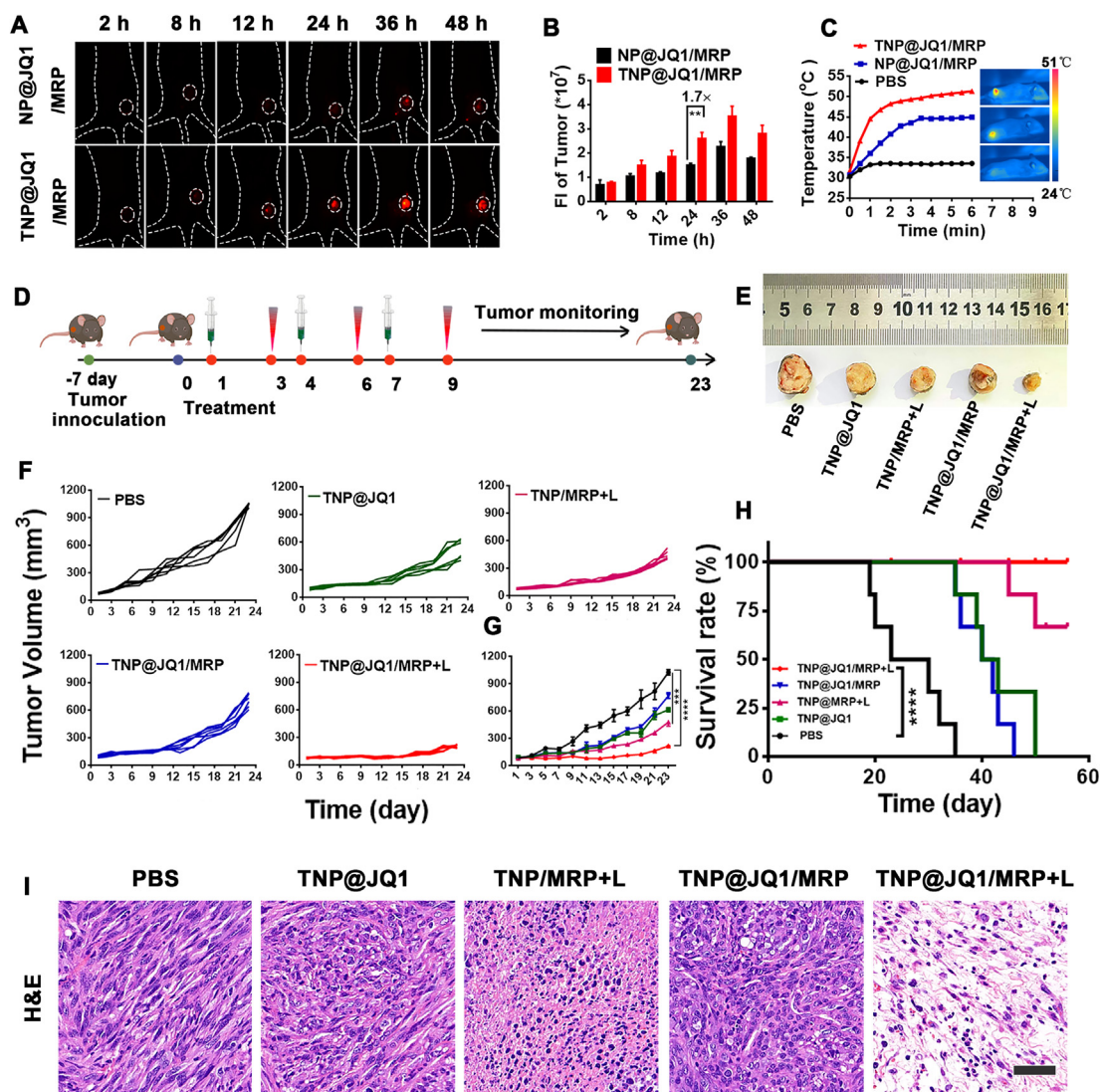
Figure 5 Antitumor efficacy of the dual-targeting nanoparticles in subcutaneous GBM tumor model. (A) NIR-II fluorescence imaging of NP@JQ1/MRP and TNP@JQ1/MRP biodistribution in G422 subcutaneous tumor-bearing mouse model *in vivo*, and (B) semi-quantitative analysis of NIR-II fluorescence intensity ($n = 3$). (C) Representative infrared thermal images of G422 subcutaneous tumor model ($n = 3$). (D) Treatment schedule for NP-mediated combination photo-immunotherapy of the G422 GBM tumor. (E) Representative photographs of the G422 tumors collected post different treatments. (F) Individual and (G) averaged growth curves of G422 tumor exposed to various treatments ($n = 6$). (H) Survival rates of different groups ($n = 6$). (I) H&E staining of tumor sections of different groups (scale bar = 50 μm). Statistical significance: $n = 6$, *$P < 0.05$, **$P < 0.01$, ***$P < 0.001$.

H&E staining of the tumor sections further demonstrated that TNP@JQ1/MRP + Laser efficiently induced apoptosis in the tumor cells (Fig. 5I). In addition, the weight of G422 tumor-bearing mice increased marginally during the experiment period (Supporting Information Fig. S15). H&E staining of the major organs (*i.e.*, heart, liver, spleen, lung and kidney) displayed negligible histopathological changes in all the experimental groups, presenting excellent biosafety of the prodrug nanoparticles (Supporting Information Fig. S16).

3.5. Immune assay in G422 subcutaneous tumor model

To clarify the mechanism underlying the excellent antitumor ability of TNP@JQ1/MRP nanoparticle-based photo-immuno-therapy, the PTT-activated immune response and JQ1-inhibited immune resistance were subsequently investigated. Flow cytometry assay showed that combination treatment with TNP@JQ1/MRP + Laser induced 4.2-fold higher matured DCs ratio in LNs compared with the PBS group (Fig. 6A and Supporting Information Fig. S17A), suggesting TNP@JQ1/MRP + Laser could efficiently elicit an immune response *in vivo*.

T lymphocyte-mediated adaptive cellular immunity is crucial for cancer immunotherapy. We thus investigated the performance of the prodrug nanoparticles for T lymphocyte activation and intratumoral accumulation by flow cytometry measurements. TNP@JQ1/MRP + Laser dramatically promoted intratumoral infiltration of CD3$^+$ T cells as well as elicited the protective immunity responses (Fig. 6B and Fig. S17B). For instance, the ratio of CD8$^+$ to CD4$^+$ T cells of the TNP/MRP + Laser and TNP@JQ1/MRP + Laser groups were 10.7- and 17.7-fold higher
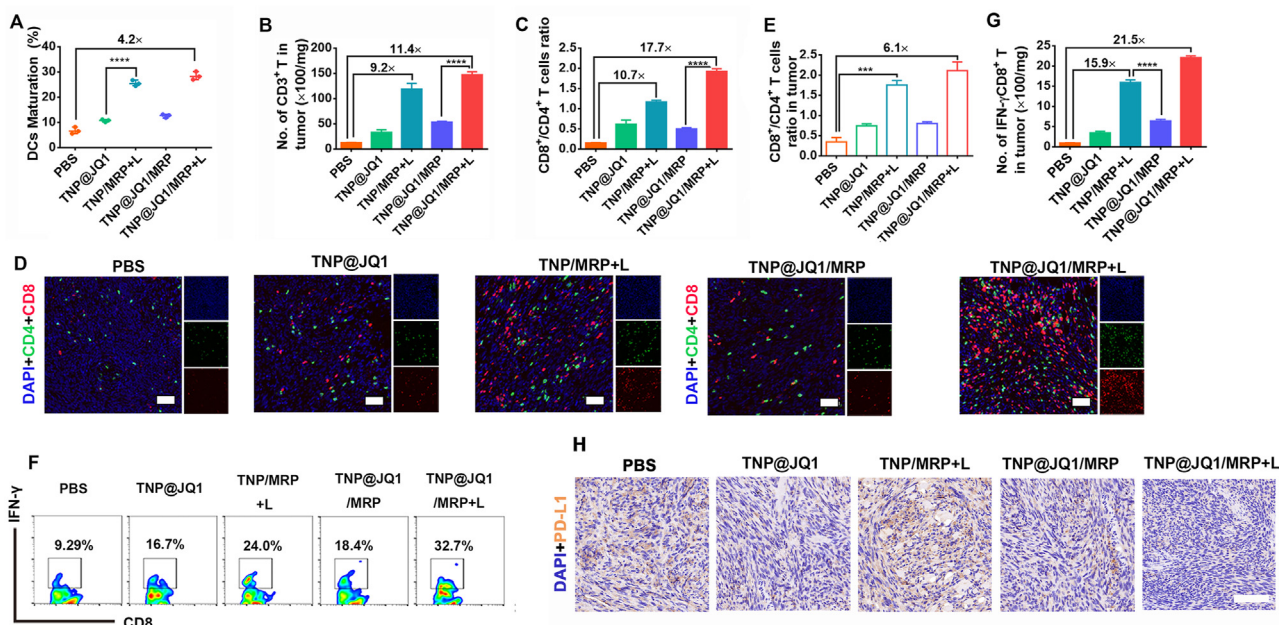
Figure 6 Mechanism of photo-immunotherapy in G422 subcutaneous tumor model. (A) Flow cytometry assay of DCs maturation in the LNs. (B) Number of the intratumor infiltration of CD3$^+$ T cells after normalization of tumor mass. (C) The ratio of the intratumor infiltration of CD8$^+$ to CD4$^+$ T cells. (D) The representative immunofluorescence images of the intratumor infiltration of CD8$^+$ and CD4$^+$ T cells (scale bar = 100 μm) and (E) the ratio of CD8$^+$ to CD4$^+$ T cells in tumor sections. (F) Flow cytometry assays of IFN-γ$^+$CD8$^+$ effector T cells. (G) Number of the intratumor infiltration of IFN-γ$^+$CD8$^+$ effector T cells after normalization of tumor mass. (H) IHC assays of PD-L1 expression (scale bar = 50 μm). Statistical significance: $n = 3$, *$P < 0.05$, **$P < 0.01$, ***$P < 0.001$.

than that of the PBS group, respectively. The successful recruitment of T lymphocytes was demonstrated by immunofluorescence staining of the tumor sections (Fig. 6C−E, and Supporting Information Figs. S17C and D). Apart from increased intratumoral infiltration of CD8$^+$ T cells, the tumor-infiltrating effector T lymphocytes (*i.e.*, IFN-γ$^+$CD8$^+$ T cells) also remarkably increased in the TNP@JQ1/MRP + Laser group, which was 21.5-fold higher than the PBS group (Fig. 6F and G), verifying photo-immunotherapy with the dual-targeting prodrug nanoparticle vigorously boosted the protective immune system.

To further investigate whether TNP@JQ1/MRP nanoparticles could circumvent IFN-γ-elicited immunity evasion *in vivo*, intratumoral PD-L1 expression was detected by immunohistochemical (IHC) assay. PD-L1 expression in TNP/MRP + Laser group dramatically increased than that of the PBS group due to increased IFN-γ secretion after PTT treatment. In contrast, combination treatment with TNP@JQ1/MRP + Laser dramatically inhibited PD-L1 expression (Fig. 6H). The above data revealed the accumulative efficacy of PTT and JQ1 to promoting the antitumor immunity cycle.

4. Conclusions

In the current study, we reported a dual-targeting nanotheranostic for photo-immunotherapy of GBM. Fluorescence and bioluminescence imaging demonstrated that the versatile TNP@JQ1/MRP nanoparticles precisely accumulated at the GBM area and diffused throughout the GBM tumor. The nanoparticles enabled precise initiation of the antitumor immune response *via* PTT-induced antigen release and NIR-II fluorescence imaging-guided photothermal therapy. The reduction-sensitive JPC prodrug eliminated IFN-γ-inducible immune evasion of the tumor cells, and the T7

peptide actively crossed the BBB and targeted the GBM tumor cells. Combinatory immunotherapy with JQ1 and PTT prominently suppressed tumor growth and prolonged the survival time in the subcutaneous G422 tumor model. The immune analysis further revealed that TNP@JQ1/MRP treatment efficiently boosted systemic antitumor immune response and recruited tumor-infiltrating CTLs for tumor regression. This study might provide a new avenue for precise photo-immunotherapy of GBM.

Author contributions

Fenglin Li, Yi Lai, Jiayi Ye and Zhiai Xu conceived the project and designed the study. Fenglin Li, Yi Lai and Jiayi Ye performed the experiments and prepared the initial manuscript. Yijing Dang and Zhifeng Zou contributed to data analysis. Madiha Saeed, Fangmin Chen and Wen Zhang helped to revise the manuscript.

Conflicts of interest

No conflict of interest to disclose.

Appendix A. Supporting information

Supporting data to this article can be found online at https://doi.org/10.1016/j.apsb.2022.05.016.

References

1. Lim M, Xia Y, Bettegowda C, Weller M. Current state of immunotherapy for glioblastoma. *Nat Rev Clin Oncol* 2018;**15**:422−42.
2. Reifenberger G, Wirsching HG, Knobbe-Thomsen CB, Weller M. Advances in the molecular genetics of gliomas-implications for classification and therapy. *Nat Rev Clin Oncol* 2017;**14**:434−52.
3. Kreth FW, Thon N, Simon M, Westphal M, Schackert G, Nikkhah G, et al. German Glioma N. Gross total but not incomplete resection of glioblastoma prolongs survival in the era of radiochemotherapy. *Ann Oncol* 2013;**24**:3117−23.
4. Beiko J, Suki D, Hess KR, Fox BD, Cheung V, Cabral M, et al. IDH1 mutant malignant astrocytomas are more amenable to surgical resection and have a survival benefit associated with maximal surgical resection. *Neuro Oncol* 2014;**16**:81−91.
5. Arvanitis CD, Ferraro GB, Jain RK. The blood−brain barrier and blood−tumour barrier in brain tumours and metastases. *Nat Rev Cancer* 2020;**20**:26−41.
6. Steeg PS. The blood−tumour barrier in cancer biology and therapy. *Nat Rev Clin Oncol* 2021;**18**:696−714.
7. Hou B, Zhou L, Wang H, Saeed M, Wang D, Xu Z, et al. Engineering stimuli-activatable boolean logic prodrug nanoparticles for combination cancer immunotherapy. *Adv Mater* 2020;**32**:1907210.
8. Kalbasi A, Ribas A. Tumour-intrinsic resistance to immune checkpoint blockade. *Nat Rev Immunol* 2020;**20**:25−39.
9. Wang W, Jin Y, Liu X, Chen F, Zheng X, Liu T, et al. Endogenous stimuli-activatable nanomedicine for immune theranostics for cancer. *Adv Funct Mater* 2021;**31**:2100386.
10. Gao J, Wang W, Pei Q, Lord MS, Yu H. Engineering nanomedicines through boosting immunogenic cell death for improved cancer immunotherapy. *Acta Pharmacol Sin* 2020;**41**:986−94.
11. Yang B, Gao J, Pei Q, Xu H, Yu H. Engineering prodrug nanomedicine for cancer immunotherapy. *Adv Sci* 2020;**7**:2002365.
12. Hu X, Hou B, Xu Z, Saeed M, Sun F, Gao Z, et al. Supramolecular prodrug nanovectors for active tumor targeting and combination immunotherapy of colorectal cancer. *Adv Sci* 2020;**7**:1903332.
13. Sun F, Zhu Q, Li T, Saeed M, Xu Z, Zhong F, et al. Regulating glucose metabolism with prodrug nanoparticles for promoting photo-immunotherapy of pancreatic cancer. *Adv Sci* 2021;**8**:2002746.
14. Ye J, Hou B, Chen F, Zhang S, Xiong M, Li T, et al. Bispecific prodrug nanoparticles circumventing multiple immune resistance mechanisms for promoting cancer immunotherapy. *Acta Pharm Sin B* 2022;**12**:2695.
15. Zhou F, Gao J, Xu Z, Li T, Gao A, Sun F, et al. Overcoming immune resistance by sequential prodrug nanovesicles for promoting chemo-immunotherapy of cancer. *Nano Today* 2021;**36**:101025.
16. Wang D, Wang T, Liu J, Yu H, Jiao S, Feng B, et al. Acid-activatable versatile micelleplexes for PD-L1 blockade-enhanced cancer photo-dynamic immunotherapy. *Nano Lett* 2016;**16**:5503−13.
17. Zhu Q, Sun F, Li T, Zhou M, Ye J, Ji A, et al. Engineering oxaliplatin prodrug nanoparticles for second near-infrared fluorescence imaging-guided immunotherapy of colorectal cancer. *Small* 2021;**17**:2007882.
18. Zhou F, Gao J, Tang Y, Zou Z, Jiao S, Zhou Z, et al. Engineering chameleon prodrug nanovesicles to increase antigen presentation and inhibit PD-L1 expression for circumventing immune resistance of cancer. *Adv Mater* 2021;**33**:2102668.
19. Ramaglia V, Rojas O, Naouar I, Gommerman JL. The ins and outs of central nervous system inflammation-lessons learned from multiple sclerosis. *Annu Rev Immunol* 2021;**39**:199−226.
20. McGranahan T, Therkelsen KE, Ahmad S, Nagpal S. Current state of immunotherapy for treatment of glioblastoma. *Curr Treat Options Oncol* 2019;**20**:24.
21. Saeed M, Chen F, Ye J, Shi Y, Lammers T, De Geest BG, et al. From design to clinic: engineered nanobiomaterials for immune normalization therapy of cancer. *Adv Mater* 2021;**33**:2008094.
22. Sun H, Zhang Q, Li J, Peng S, Wang X, Cai R. Near-infrared photoactivated nanomedicines for photothermal synergistic cancer therapy. *Nano Today* 2021;**37**:101073.
23. Chen Q, Xu L, Liang C, Wang C, Peng R, Liu Z. Photothermal therapy with immune-adjuvant nanoparticles together with checkpoint blockade for effective cancer immunotherapy. *Nat Commun* 2016;**7**:13193.
24. Lin H, Gao S, Dai C, Chen Y, Shi J. A two-dimensional biodegradable niobium carbide (MXene) for photothermal tumor eradication in NIR-I and NIR-II biowindows. *J Am Chem Soc* 2017;**139**:16235−47.
25. Matos TR, Sheth V. The symbiosis of phototherapy and photo-immunology. *Clin Dermatol* 2016;**34**:538−47.
26. Nam J, Son S, Ochyl LJ, Kuai R, Schwendeman A, Moon JJ. Chemo-photothermal therapy combination elicits anti-tumor immunity against advanced metastatic cancer. *Nat Commun* 2018;**9**:1074.
27. Wang C, Xu L, Liang C, Xiang J, Peng R, Liu Z. Immunological responses triggered by photothermal therapy with carbon nanotubes in combination with anti-CTLA-4 therapy to inhibit cancer metastasis. *Adv Mater* 2014;**26**:8154−62.
28. Zhu X, Wan H, Jia H, Liu L, Wang J. Porous Pt nanoparticles with high near-infrared photothermal conversion efficiencies for photothermal therapy. *Adv Healthc Mater* 2016;**5**:3165−72.
29. Lai Y, Dang Y, Li F, Ding C, Yu H, Zhang W, Xu Z. Reactive glycolysis metabolite-activatable nanotheranostics for NIR-II fluorescence imaging-guided phototherapy of cancer. *Adv Funct Mater* 2022;**32**:2200016.
30. Chen W, Qin M, Chen X, Wang Q, Zhang Z, Sun X. Combining photothermal therapy and immunotherapy against melanoma by polydopamine-coated Al_2O_3 nanoparticles. *Theranostics* 2018;**8**:2229−41.
31. Anraku Y, Kuwahara H, Fukusato Y, Mizoguchi A, Ishii T, Nitta K, et al. Glycaemic control boosts glucosylated nanocarrier crossing the BBB into the brain. *Nat Commun* 2017;**8**:1001.
32. Jia Y, Wang X, Hu D, Wang P, Liu Q, Zhang X, et al. Photo-theranostics: active targeting of orthotopic glioma using biomimetic proteolipid nanoparticles. *ACS Nano* 2019;**13**:386−98.
33. Lam FC, Morton SW, Wyckoff J, Vu Han TL, Hwang MK, Maffa A, et al. Enhanced efficacy of combined temozolomide and bromodomain inhibitor therapy for gliomas using targeted nanoparticles. *Nat Commun* 2018;**9**:1991.
34. Yang X, Yang S, Chai H, Yang Z, Lee RJ, Liao W, et al. A novel isoquinoline derivative anticancer agent and its targeted delivery to tumor cells using transferrin-conjugated liposomes. *PLoS One* 2015;**10**:0136649.
35. Yang Z, Du Y, Sun Q, Peng Y, Wang R, Zhou Y, et al. Albumin-based nanotheranostic probe with hypoxia alleviating potentiates synchronous multimodal imaging and phototherapy for glioma. *ACS Nano* 2020;**14**:6191−212.
36. Zhang M, Wang W, Mohammadniaei M, Zheng T, Zhang Q, Ashley J, et al. Upregulating aggregation-induced-emission nanoparticles with blood-tumor-barrier permeability for precise photothermal eradication of brain tumors and induction of local immune responses. *Adv Mater* 2021;**33**:2008802.
37. Oh S, Kim BJ, Singh NP, Lai H, Sasaki T. Synthesis and anti-cancer activity of covalent conjugates of artemisinin and a transferrin-receptor targeting peptide. *Cancer Lett* 2009;**274**:33−9.
38. Bi Y, Liu L, Lu Y, Sun T, Shen C, Chen X, et al. T7 peptide-functionalized PEG-PLGA micelles loaded with carmustine for targeting therapy of glioma. *ACS Appl Mater Interfaces* 2016;**8**:27465−73.
39. Wang Y, Lin T, Zhang W, Jiang Y, Jin H, He H, et al. A prodrug-type, MMP-2-targeting nanoprobe for tumor detection and imaging. *Theranostics* 2015;**5**:787−95.
40. Wang Z, Zhao Y, Jiang Y, Lv W, Wu L, Wang B, et al. Enhanced anti-ischemic stroke of ZL006 by T7-conjugated PEGylated liposomes drug delivery system. *Sci Rep* 2015;**5**:12651.

41. Chen R, Liu F, Qiu X, Chen X. The prognostic and therapeutic value of PD-L1 in glioma. *Front Pharmacol* 2018;**9**:1503.

42. Wang Z, Zhang C, Liu X, Wang Z, Sun L, Li G, et al. Molecular and clinical characterization of PD-L1 expression at transcriptional level *via* 976 samples of brain glioma. *OncoImmunology* 2016;**5**:1196310.

43. Zhong Y, Dai H. A mini-review on rare-earth down-conversion nanoparticles for NIR-II imaging of biological systems. *Nano Res* 2020;**13**:1281−94.

44. Antaris AL, Chen H, Cheng K, Sun Y, Hong G, Qu C, et al. A small-molecule dye for NIR-II imaging. *Nat Mater* 2016;**15**:235−42.

45. Korb E, Herre M, Zucker-Scharff I, Darnell RB, Allis CD. BET protein Brd 4 activates transcription in neurons and BET inhibitor Jq1 blocks memory in mice. *Nat Neurosci* 2015;**18**:1464−73.

46. Shi B, Ren N, Gu L, Xu G, Wang R, Zhu T, et al. Theranostic nanoplatform with hydrogen sulfide activatable NIR responsiveness for imaging-guided on-demand drug release. *Angew Chem Int Ed* 2019;**58**:16826−30.

47. Zhu C, Huo D, Chen Q, Xue J, Shen S, Xia Y. A eutectic mixture of natural fatty acids can serve as the gating material for near-infrared-triggered drug release. *Adv Mater* 2017;**29**:1703702.